#### **PAPER • OPEN ACCESS**

# Wind LiDAR Measurements of Wind Turbine Wakes Evolving over Flat and Complex Terrains: Ensemble Statistics of the Velocity Field

To cite this article: Lu Zhan et al 2020 J. Phys.: Conf. Ser. 1452 012077

View the <u>article online</u> for updates and enhancements.



## IOP ebooks™

Bringing together innovative digital publishing with leading authors from the global scientific community.

Start exploring the collection-download the first chapter of every title for free.

NAWEA WindTech 2019

**1452** (2020) 012077 doi:10.1088/1742-6596/1452/1/012077

### Wind LiDAR Measurements of Wind Turbine Wakes Evolving over Flat and Complex Terrains: Ensemble Statistics of the Velocity Field

#### Lu Zhan, Stefano Letizia and Giacomo Valerio Iungo

Wind Fluids and Experiments (WindFluX) Laboratory, Mechanical Engineering Department, The University of Texas at Dallas, Richardson, 75080 TX, USA

E-mail: valerio.iungo@utdallas.edu

Abstract. Wind velocity measurements of wakes generated by utility-scale wind turbines were performed with the University of Texas at Dallas (UTD) mobile LiDAR station for wind farms in flat and complex terrains. Single-wake LiDAR measurements are clustered according to incoming wind speed at hub height and atmospheric stability regime through the wind shear exponent. Ensemble statistics of the LiDAR data shows that the velocity field in the near-wake is mainly affected by the rotor thrust coefficient, while atmospheric stability is the prevailing factor governing wake recovery. For the wind farm in complex terrain, the wind field is significantly affected by the local orography, showing either local speed-up or low-velocity regions. The analysis of the SCADA data corroborates the occurrence of these wind features and enables quantifying their effects on the wind plant performance.

#### 1. Introduction

Power losses due to turbine wake interactions represent a major concern for the wind energy industry. Average power losses about 10-20% have been reported for large offshore wind farms [1], while short-term power losses can even exceed 80% of the expected value for single turbines in onshore wind farms under specific wind conditions, with a total loss on AEP of 2.4% and 4% during nighttime stable and daytime convective regimes, respectively [2]. Therefore, accurate modeling of wakes and their interactions is of utmost importance for design and operations of wind parks [3, 4, 5]. Previous works highlighted the important role of atmospheric stability in the wake evolution and recovery [2, 6, 7]. Indeed, the surface heat flux can act as turbulence source (sink) during daytime unstable conditions (nighttime stable conditions) and, thus, promote (delay) turbulent mixing and wake recovery.

More recently, large wind farms have been built on complex terrains [8] where the interaction of the atmospheric boundary layer with orography generates a variety of micro-scale phenomena such as speed-up, recirculation zones, internal waves, low momentum streaks and local flow distortion [9]. The investigation of these flow features is extremely complicated due to the large Reynolds number, the irregular topography, the uncertain boundary conditions and the influence of Coriolis and buoyancy forces.

With the aim of investigating wind turbine wake morphology and wake interactions, we performed two LiDAR campaigns: the first experiment took place at a wind farm in North Texas installed over a flat terrain, while the second campaign was carried out for a wind farm

Content from this work may be used under the terms of the Creative Commons Attribution 3.0 licence. Any further distribution of this work must maintain attribution to the author(s) and the title of the work, journal citation and DOI.

Published under licence by IOP Publishing Ltd

**1452** (2020) 012077 doi:10.1088/1742-6596/1452/1/012077

in complex terrain located in North-East Colorado. For the first experiment, the daily cycle of the atmospheric stability is the driving factor for wake evolution, while for the tests in complex terrain, a sharp escarpment surrounding the wind farm gives rise to local speed-up and low momentum regions that significantly affect wind turbine performance.

This paper is structured as follows: the sites of the experiments and the instrumentation are described in section 2. The LiDAR data post-processing and clustering are reported in section 3 together with the main results for the flat-terrain wind farm. In section 4, experimental evidences of the effects of topography on the flow pattern in complex terrain is provided, also including the quantification of power and energy losses via SCADA-data analysis. Finally, concluding remarks are given in section 5.

#### 2. Experimental setup and site description

Our experimental strategy consists in collecting a statistically-significant amount of LiDAR data under a broad range of atmospheric and turbine-operative conditions to perform a cluster analysis of wind turbine wakes. To this aim, the UTD mobile LiDAR station was deployed in two wind farms: one in Texas over flat terrain and another one in Colorado over complex terrain (Fig. 1). The LiDAR station includes a WindCube 200S pulsed scanning Doppler wind LiDAR, two Campbell Scientific CSAT3 sonic anemometers and a remotely controlled station for monitoring, scan implementation and data acquisition. More details about the experimental equipment can be found in [2].

The first LiDAR campaign was conducted from August 2015 to March 2017 in a wind farm in North Texas consisting of 25 Siemens SWT-2.3-108 wind turbines (Table 1). The turbines are arranged in three rows oriented along the East-West direction, perpendicularly to the prevailing wind direction. Sonic anemometers are mounted on a meteorological (met) tower at heights of 36 m, 60 m and 80 m, which provide data for calculating the wind shear exponent and air density correction according to IEC standard [10]. Moreover, 10-minute statistics (mean, standard deviation, minimum, maximum) of operational data are collected and stored from the SCADA.

The second experimental campaign was carried out from May to December 2018 in a wind farm located in North-East Colorado, including 221 Mitsubishi MWT-1000-61 and 53 GE sle1.5 wind turbines, for an overall installed capacity of 300.5 MW (Table 1). All the generators are installed on a relatively flat plateau protruding from the surrounding plain by roughly 80 m. The detailed topographic map with a resolution  $10 \text{ m} \times 7 \text{ m}$ , provided by the U.S. Geological Survey [11], is shown in Fig. 2, along with the farm layout. The turbines rows are approximately aligned perpendicularly to the NW-SE direction, the latter being the prevailing wind direction, as indicated by the site wind rose in Fig. 2 c.

Two met-towers are installed in the northern side of the power plant, which are equipped

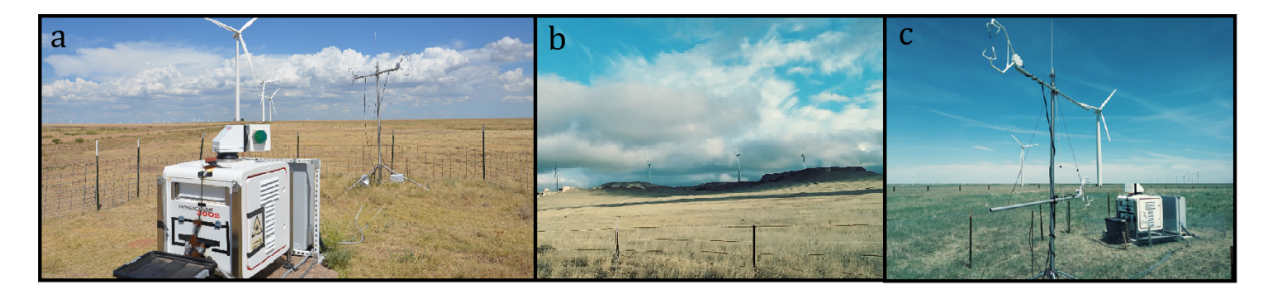


**Figure 1.** Deployments of the UTD mobile LiDAR station: a) wind farm in North Texas; b) Escarpment surrounding the wind farm in Colorado; c) wind farm in Colorado.

**1452** (2020) 012077

doi:10.1088/1742-6596/1452/1/012077

	SWT-2.3-108	MWT-1000-61	GE sle1.5
Terrain type	Flat	Complex	Complex
Rated power [kW]	2300	1000	1500
Cut-in wind speed [m/s]	3-4	3.5	3.5
Cut-out wind speed [m/s]	25	25	25
Rated wind speed [m/s]	11-12	13.5	14
Type	Variable speed-pitch	Variable pitch	Variable speed-pitch
Hub height [m]	78.4	69	80
Rotor diameter [m]	108	61.4	77

Table 1. Technical specifications of the wind turbines under investigation.

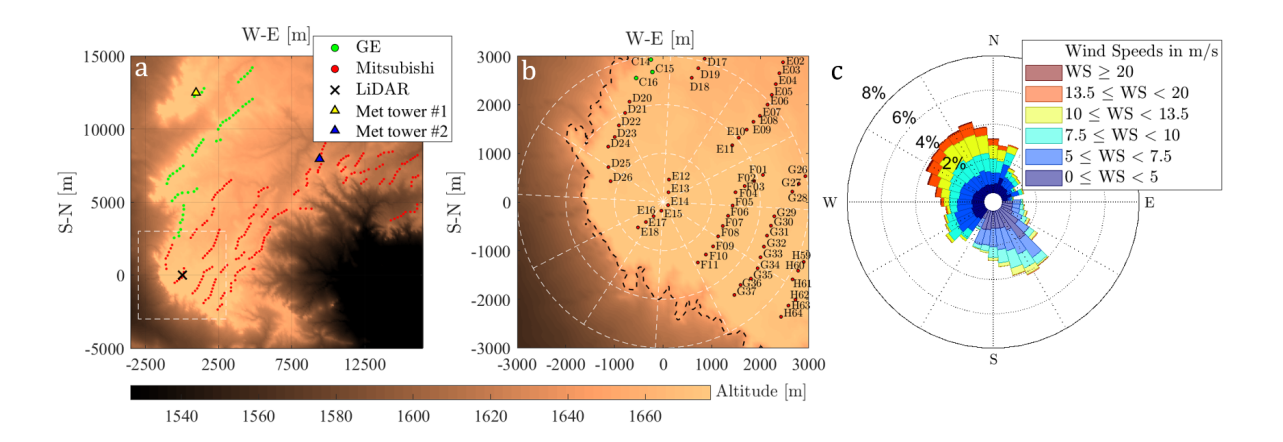


**Figure 2.** Wind farm in Colorado: a) topographic map; b) turbines monitored with the LiDAR; c) wind rose from both met towers. The wind sectors with shaded colors represent regions with potential wake interactions.

with two anemometers and directional vanes at two heights (50 m and 80 m for the met-tower #1, 50 m and 69 m for the met-tower #2, as indicated in Fig. 2). Pressure and temperature probes are also installed at a single height. Meteorological data are stored in terms of average, standard deviation, maximum and minimum values for sampling periods of 10 minutes. SCADA data (wind speed, nacelle orientation, power, RPM, blade pitch) are recorded for each turbine and stored with the same time resolution and format of the met-data. For the entire duration of the deployment, the LiDAR was installed at the origin of the reference system of Fig. 2 a and remained operative for 197 days.

#### 3. Wind farm on flat terrain

More than 9000 single wake planar-position indicator (PPI) scans were collected, post-processed and clustered according to the density-corrected incoming wind speed (see [10]) and wind shear exponent before calculating ensemble statistics of the wake velocity field. Doppler LiDAR is a one-dimensional instrument measuring the radial velocity, which is the projection of the wind speed along the direction of the LiDAR laser beam. Provided an estimation of the wind direction,  $\theta_w$ , which is obtained directly from the LiDAR data, we can calculate a proxy for the horizontal streamwise velocity, which is denoted as equivalent velocity:

$$U_{eg} \sim V_r / \left[ \cos\phi \cos(\theta - \theta_w) \right],$$
 (1)

**1452** (2020) 012077 doi:10.1088/1742-6596/1452/1/012077

where  $\phi$  and  $\theta$  are the elevation and azimuthal angles, respectively, of the LiDAR laser beam. For this study,  $\theta_w$  is approximated with the wake direction, which is estimated through the linear fitting of the wake centers measured at various downstream locations. The elevation angle for the PPI scans,  $\phi$ , was set typically between 3° and 4° (occurrence 77%), seldom in the range 2°-3° (occurrence 7.5%) or 4°-5° (occurrence 15.5%).

In order to remove effects of wind variability on the wake analysis, the LiDAR velocity fields are normalized by the incoming vertical profile of the horizontal wind speed of the respective PPI scan,  $U_{eq}^* = U_{eq}/U_{\infty}$ , where the freestream vertical profile,  $U_{\infty}$ , is evaluated from the LiDAR measurements not affected by the wakes. The transverse position of the wake center at each downstream location is estimated by fitting  $U_{eq}$  with a Gaussian function. Since  $U_{eq}$  is a function of the wake direction (Eq. 1), and  $U_{eq}$  is post-processed to estimate the wake direction, an iterative procedure is then implemented to estimate both  $U_{eq}$  and  $\theta_w$ . Convergence of this iterative method is achieved when consecutive iterations produce a modification of  $\theta_w$  lower than 0.1°. The PPI scans are subsequently analyzed within a reference frame with the x-direction coincident with the  $\theta_w$ -direction.

Each PPI scan is associated with synchronized 10-minute averaged SCADA and met tower data, from which it is possible to retrieve parameters, such as the density-corrected normalized wind speed,  $U_{hub}^*$ , and wind shear exponent,  $\alpha$ . In this study, five clusters based on incoming wind speed are selected by using the following boundary values: 0.35, 0.53, 0.71, 0.85, 1, 1.14. These values have been selected to single out the wake variability as a function of wind turbine settings and, in turn, power and thrust.

Similarly to a previous LiDAR experiment performed at the same wind farm under investigation [2], the atmospheric stability regime is characterized through the wind shear exponent,  $\alpha$ . Specifically, convective conditions are characterized by  $\alpha < 0.2$ , while stable conditions by  $\alpha > 0.3$ . Wind conditions between these two classes  $(0.2 \le \alpha \le 0.3)$  are classified as neutral conditions and not analyzed in order to sharpen the results as a function of atmospheric stability. The shear exponent is calculated through the met-tower data with the wind speed measured at two different heights, namely 60 m and 80 m, as follows:

$$\alpha = \log(U_2/U_1)/\log(z_2/z_1). \tag{2}$$

LiDAR wake measurements are clustered as function of the incoming wind speed at hub height measured by the SCADA and wind shear exponent. Ensemble statistics of the wake velocity field for each cluster are then calculated through the Barnes' scheme [13, 14], which can be considered as a spatial-averaging technique to generate a mean wake velocity field from the scattered LiDAR data (see Fig. 3).

To project the inclined PPI data into the horizontal plane at hub height, the Cartesian reference frame of the LiDAR measurements is converted into a cylindrical reference frame with unchanged x-direction. The radial coordinate is calculated with sign in order to discern the two sides of the wake, as follows:

$$r = \frac{(y - y_c)}{|y - y_c|} \sqrt{(y - y_c)^2 + z^2},$$
(3)

where  $y_c$  is the transverse coordinate of the wake center. For each grid point  $(x_j, r_i)$ , the average velocity field is calculated through the Barnes' scheme as follows:

$$\overline{U_{eq}^*}(x_j, r_i) = \frac{\sum_{k=1}^n U_{eq}^*(x_k, r_k) w_k(x_j) w_k(r_i)}{\sum_{k=1}^n w_k(x_j) w_k(r_i)}$$
(4)

where n is the total number of LiDAR samples falling within the grid cell with centroid  $(x_j, r_i)$ , while the streamwise weighting function is given by:

$$w_k(x_j) = e^{-\frac{(x_j - x_k)^2}{2\sigma_x^2}} \tag{5}$$

**1452** (2020) 012077

doi:10.1088/1742-6596/1452/1/012077

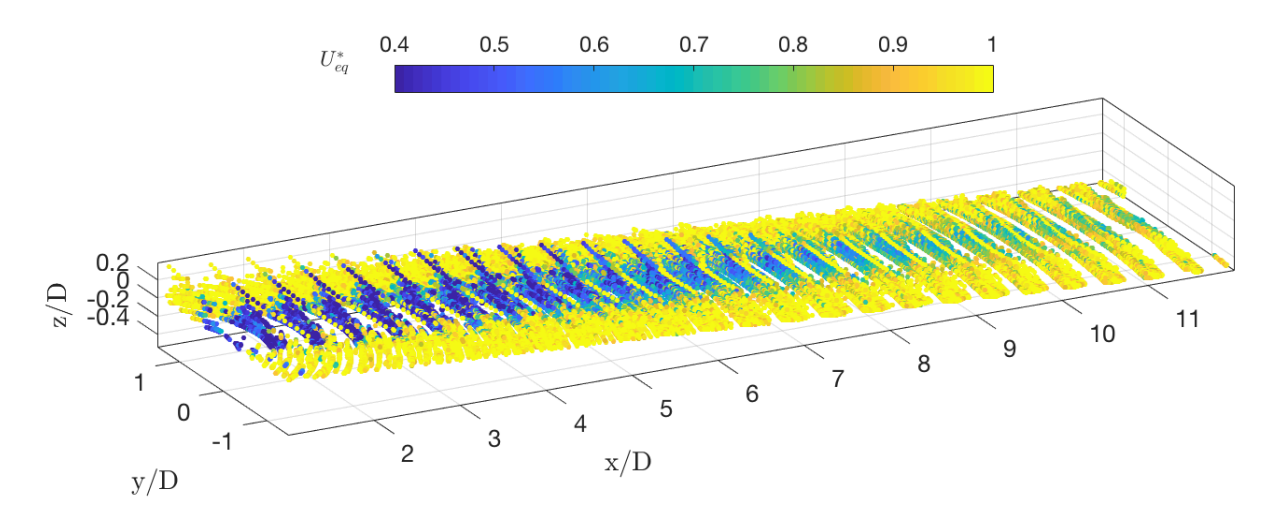


**Figure 3.** Non-dimensional PPI data of the cluster with  $U_{hub}^* \in [0.71, 0.85]$  and  $\alpha \in [0.3, 0.55]$ .

and the radial weighting function is:

$$w_k(r_i) = e^{-\frac{(r_i - r_k)^2}{2\sigma_r^2}} \tag{6}$$

The standard deviation of the two weighting functions is set equal to the respective grid resolutions, dx and dr, multiplied by a factor  $\beta = 2.8$ , which has been selected upon sensitivity analysis. The statistical significance of the ensemble statistics is ensured after the rejection of grid nodes exhibiting standard error on the weighted mean higher than 0.04.

In Fig. 4, the ensemble average of the wake velocity profiles calculated at two different downstream locations and for convective and stable stability regimes are reported. First, for  $x=1.75\ D$  and convective conditions, the typical Gaussian-like profile of the wake velocity field, which is typically used for wake models, is observed [15]. Such smooth Gaussian trend is not clearly obtained for the stable conditions where a slightly lower velocity deficit is detected on the side with negative values of the radial position (turbine rotation is in the positive x-direction). Considering that LiDAR measurements acquired during the occurrence of significant wind veer have been removed for the present data analysis, we would speculate that this flow feature is the result of the very low incoming atmospheric turbulence intensity (< 5%) and the swirling flow induced by the turbine rotation in the near-wake. Indeed, this asymmetry in the wake velocity profiles is practically not observed for the downstream location of  $x=5\ D$  where the swirling velocity in the wake is practically completely decayed [16, 17, 18].

The main variability in the wake velocity deficit is inferred by the incoming wind speed and, thus, the different values of the rotor thrust coefficient [2]. For operations between cut-in and rated wind speed  $(0.35 < U_{hub}^* < 0.85$ , region two of the power curve), the turbines should operate with a constant thrust coefficient in order to maximize power capture. However, we observe that for the first velocity cluster  $(0.35 < U_{hub}^* < 0.53)$ , a lower velocity deficit is observed with respect to the other two clusters of region two of the power curve  $(0.53 < U_{hub}^* < 0.85)$ . This indicates that in proximity of the cut-in wind speed the turbine blades do not operate at the maximum aerodynamic efficiency and thrust coefficient. In contrast, the velocity profiles for the other two clusters in region two look very similar. For incoming wind speed between rated and cut-off wind speed, namely region three of the power curve, a gradual reduction of the velocity deficit is observed, which is clearly due to the increased blade pitch angle and reduction of the thrust coefficient in order to maintain the power capture at rated value.

**1452** (2020) 012077

doi:10.1088/1742-6596/1452/1/012077

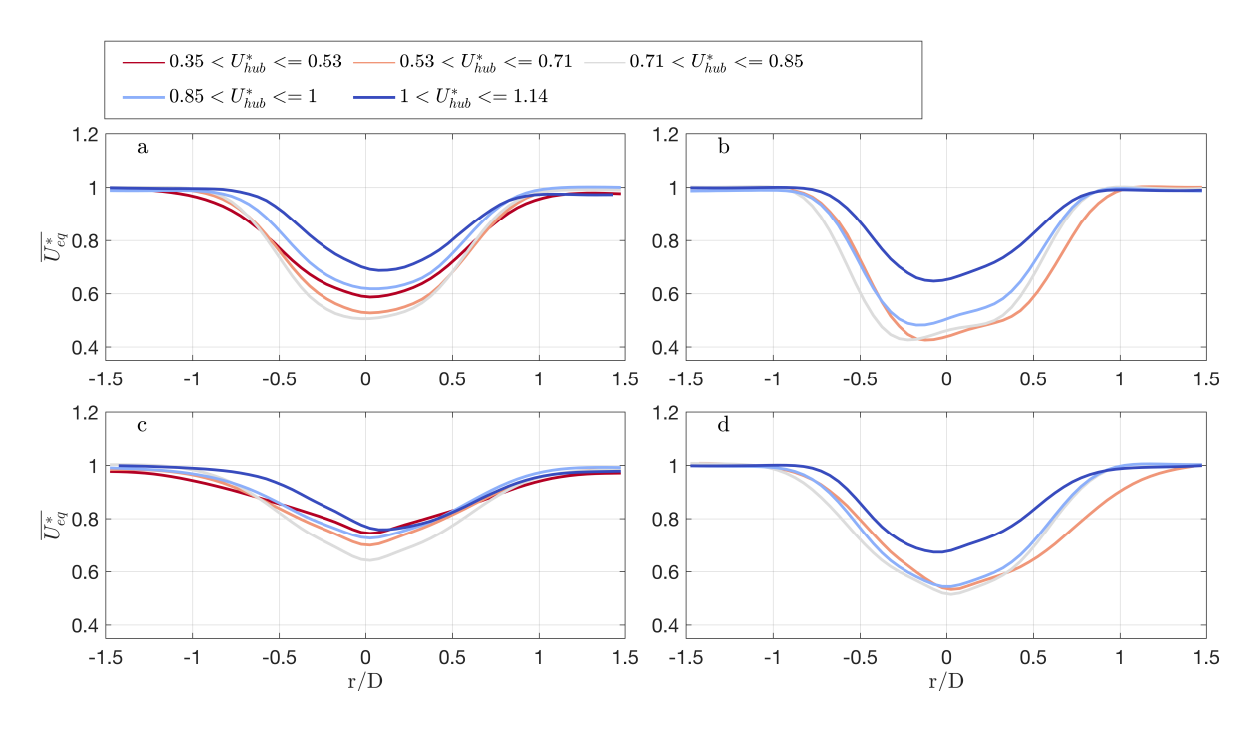


**Figure 4.** Ensemble-averaged wake velocity field: (a) x = 1.75 D under convective conditions; (b) x = 1.75 D under stable conditions; (c) x = 5 D under convective conditions; (d) x = 5 D under stable conditions.

$U^*_{hub}$	[0.35,  0.53]	[0.53, 0.71]	[0.71, 0.85]	[0.85, 1]	[1, 1.14]
Convective B parameter	0.5925	0.6849	0.6665	0.5102	0.4023
Stable B parameter	-	0.7299	0.6664	0.5967	0.3848
Convective N parameter	0.5842	0.5557	0.4113	0.4211	0.3491
Stable N parameter	-	0.3102	0.2132	0.1837	0.1102

**Table 2.** Exponential fitting results of the minimum velocity deficit  $\Delta \overline{U_{eq}^*}$ .

Already from Fig. 4, we can observe that the velocity deficit for convective conditions is lower compared to cases with the same cluster of the incoming wind speed and stable atmospheric conditions, which is the result of entrainment of ambient flow within the wake. Furthermore, Fig. 4 c and d show that after propagating the same distance downstream, the amount of the reduction of wake deficit is larger for convective conditions. Effects of atmospheric stability on downstream wake evolution are analyzed more in depth through Fig. 5, where the minimum velocity deficit,  $\Delta \overline{U_{eq}^*} = 1 - min(\overline{U_{eq}^*})$ , is calculated for various downstream locations. An exponential fitting is then carried out on the velocity deficit profiles as  $y = B(x/D)^{-N}$ , where B is the velocity deficit at x = 1 D and N represents the downstream wake recovery rate. The values obtained from the fitting procedure are reported in Table 2.

The analysis of the obtained fitting parameters confirms the enhancement of wake recovery rate under convective conditions. However, a secondary effect on wake recovery rate is singled out as a function of the incoming wind speed (Fig. 5). Given the atmospheric stability class, a faster wake recovery is observed for operations in region two of the power curve, which occur with a thrust coefficient close to the maximum value. In contrast, for operations in region three of the power curve, the increasing blade pitch angle leads to a reduced thrust coefficient and slower wake recovery due to the reduction of turbine added turbulence. This effect can be clearly

**1452** (2020) 012077 doi:10.1

doi:10.1088/1742-6596/1452/1/012077

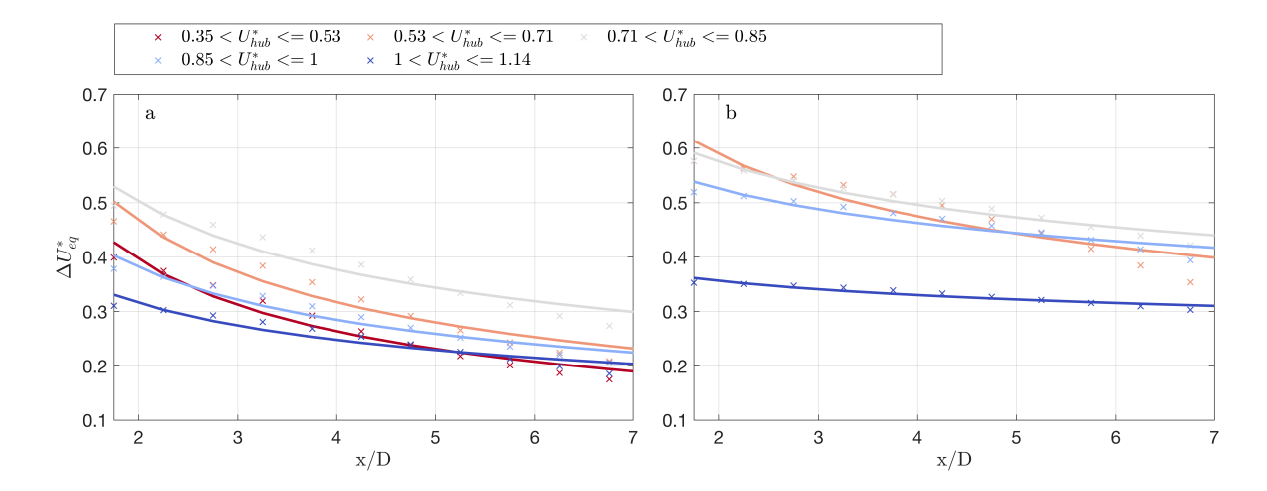


**Figure 5.** Velocity deficit as a function of the downstream location for various clusters based on incoming wind speed and atmospheric stability: (a) Convective conditions ( $0 < \alpha < 0.2$ ); (b) Stable conditions ( $0.3 < \alpha < 0.55$ ). Markers represent the LiDAR data and the solid line stands for exponential fitting of the corresponding data.

observed in Table 2, where higher values of the parameter N are estimated for region two of the power curve. This wake feature is ascribed to a different level of mechanically-generated turbulence, which is a result of the different axial shear and thrust coefficient of the wind turbine rotor.

#### 4. Wind farm on complex terrain

Full-angle PPI scans were performed to monitor the complex flow patterns evolving over the topography at a wind farm in Colorado. Scans with elevation angle between 1° and 2° are considered for this study with mean wind direction within the range [165°,170°], which corresponds to the prevailing southerly wind direction measured by the met-towers (Fig. 2c). Thirteen PPI scans are processed in terms of  $\overline{U_{eq}}$  following Eq. 1 and ensemble statistics are calculated in LiDAR spherical coordinates.  $\overline{U_{eq}}$  is then projected into the hub height horizontal plane through the wind shear of Eq. 2.

The presence of velocity acceleration at the Northwestern escarpment is evident from the LiDAR data reported in Fig. 6 a. The high-speed area around the turbines produces significantly larger wind speed and, thus, power production, which is confirmed through the power analysis in Fig. 8 a. Mitsubishi turbines in D array and General Electric turbine C16 (yellow dots in Fig. 6 a), individually generate more power than the clusters at the Southeastern corner of the layout (green dots in the same figure). Meanwhile, the Southeastern corner and central arrays experience a remarkable distorted flow due to the southern escarpment surrounding the site. This flow feature has been further investigated through a linear regression between the conditionally-averaged hub-height wind-speed measured from the SCADA and wind velocity measured by the LiDAR at an upstream distance from the turbine rotors of 2 D (Fig. 6 b). The good correlation coefficient obtained from this analysis implies the good accuracy of the ensemble averaged velocity map.

Three years of SCADA and met-data (period 2016-2018) have been analyzed to quantify the effect of topography and wake interactions on the wind farm performances. Following the

**1452** (2020) 012077 doi:10.1088/1742-6596/1452/1/012077

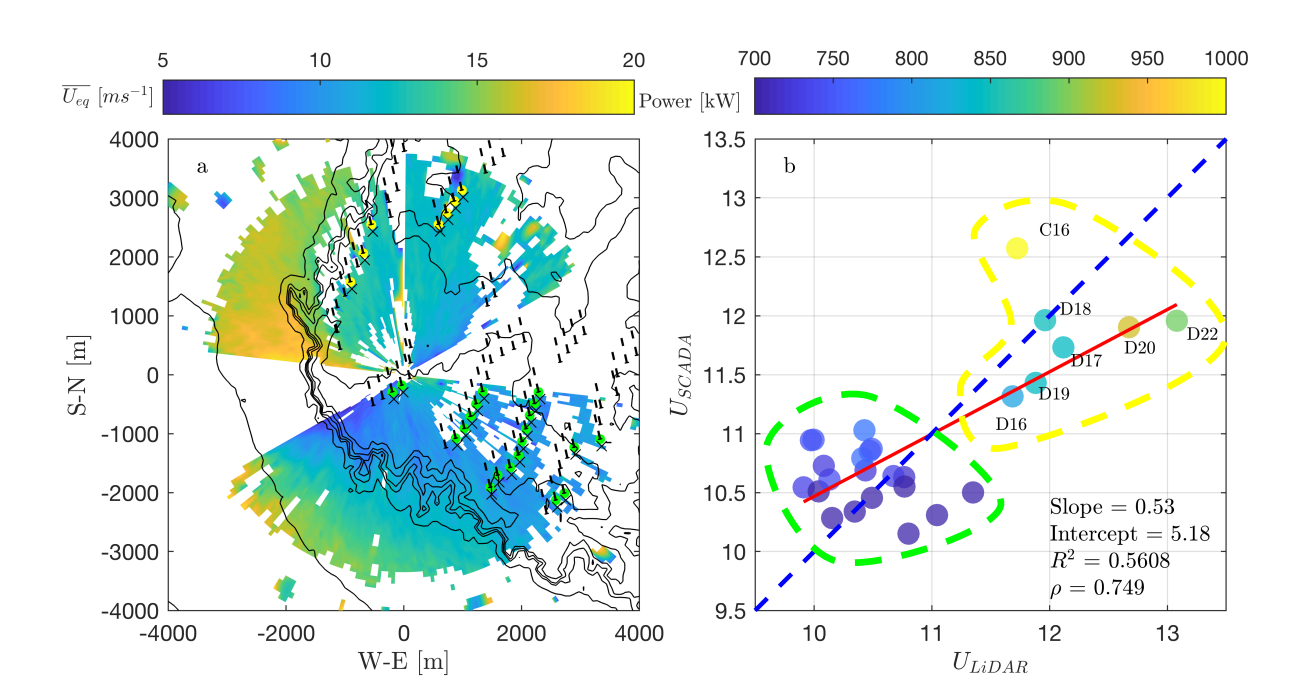


**Figure 6.** LiDAR velocity measurements for the wind farm on complex terrain: (a) velocity field retrieved over the horizontal plane at hub height. Black dashed lines mark wake trajectories. Green dots and yellow dots represent the turbines sampled for SCADA comparison and black crosses show 2-D-upstream locations; (b) linear regression between hub height velocity sampled from LiDAR and SCADA. Each dot is colored by the power production. Green and yellow dashed circles indicate turbine clusters with same colors than panel (a).

approach of [2], we define the percentage power loss of the i-th turbine as:

$$\Delta P_i(t) = \frac{P_{free,i}(t) - P_i(t)}{P_{free,i}(t)} \times 100 \tag{7}$$

where  $P_{free}$  is the ideal power capture of an isolated turbine operating under the considered wind conditions. An equivalent definition of power loss for wind farms in complex terrain is still debated in the wind energy community [19]. Among all the methods proposed in literature, such as maximum power [20], upstream power [1], cluster analysis [19], we have selected the power curve method as the most suitable for the present case [2]. According to this method, the freestream power is estimated by injecting the free-stream velocity into the normalized experimental power curve:

$$\frac{P_{free,i}}{P_{rated,i}} = f_i(U_{hub}^*) \tag{8}$$

where  $U_{hub}^*$  is the density-corrected freestream velocity [10] and  $f_i(U_{hub}^*)$  is the experimental power curve of the specific turbine. The advantages of this method are the statistical robustness, easy implementation for large and irregular arrays and the applicability to farms including different turbine models. Moreover, unlike techniques based on maximum power, the power curve method is capable of identifying (as negative power losses) turbines over-performing due to local flow speed-up.

The freestream velocity is defined as the average velocity measured by the nacelle-mounted anemometers of the "unwaked" turbines. Values of velocity outside of the range [5-th, 95-th] percentile have been discarded as likely outliers. In order to select the unwaked towers for such

**1452** (2020) 012077

doi:10.1088/1742-6596/1452/1/012077

a vast and unstructured layout, we adopted the Jensen wake model [12] with quadratic wake superposition [21]. The wake decay coefficient was calculated through the equation proposed by [22] using the median turbulence intensity from both met towers (TI = 10.7%). Turbines experiencing a velocity higher than 99% of the freestream velocity according to the Jensen model are considered as unwaked.

Power losses as a function of time have been averaged, after excluding extreme values outside of the range [5-th,95-th] percentile. In the present work, only values of freestream belonging to the region two are considered (specifically normalized velocity  $U^*_{hub} \in (0.3,1)$ ). Cases having an error on the mean based on the t-test higher than 5% of the rated power with 90% confidence are flagged as statistically insignificant and excluded.

Fig. 7 a displays the power losses only for waked sectors. The Mitsubishi turbines at the center of the plateau experience higher power losses ( $\sim 5-10\%$ ) while, unexpectedly, the turbines placed on the western escarpment produce on average more power than the estimated potential. Interestingly, the power losses for unwaked wind sector (Fig. 7 b) reveal a quite different scenario, with higher losses occurring for the Mitsubishi installed in proximity to the sharp western and south-eastern escarpments. The four areas indicated in Fig. 7 have been selected for further investigations. To better understand the dependence of the power harvesting on the wind direction, the power losses have been bin-averaged in wind sectors of amplitude  $\Delta\theta=10^\circ$ . Fig. 8 reports the directional power losses in the four selected regions. Fig. 8 a, which corresponds to the D-row Mitsubishi turbines located close to the western escarpment, shows considerable losses when the wind blows from West. Conversely, power gain is achieved for easterly winds. This striking directional behavior of the power production is most likely the result of the local topography. Apparently, the sharp western escarpment creates considerable flow disturbances

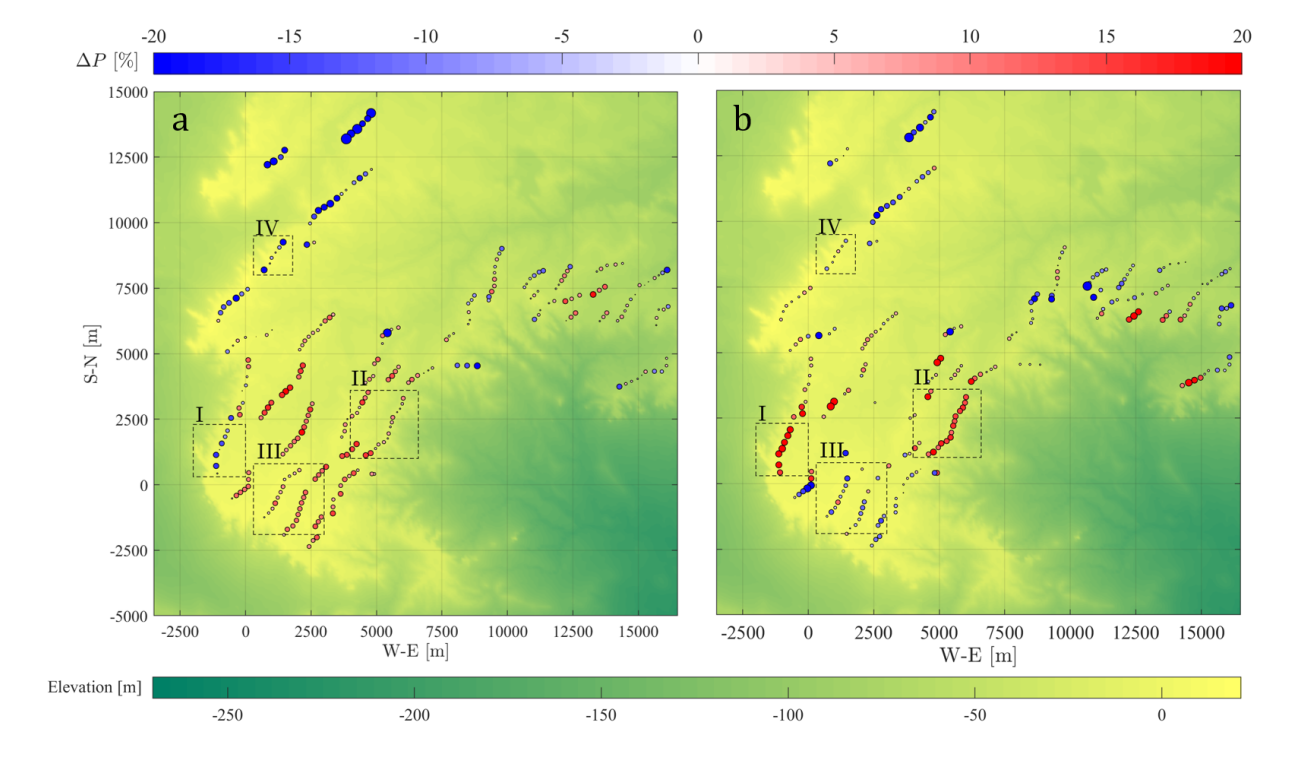
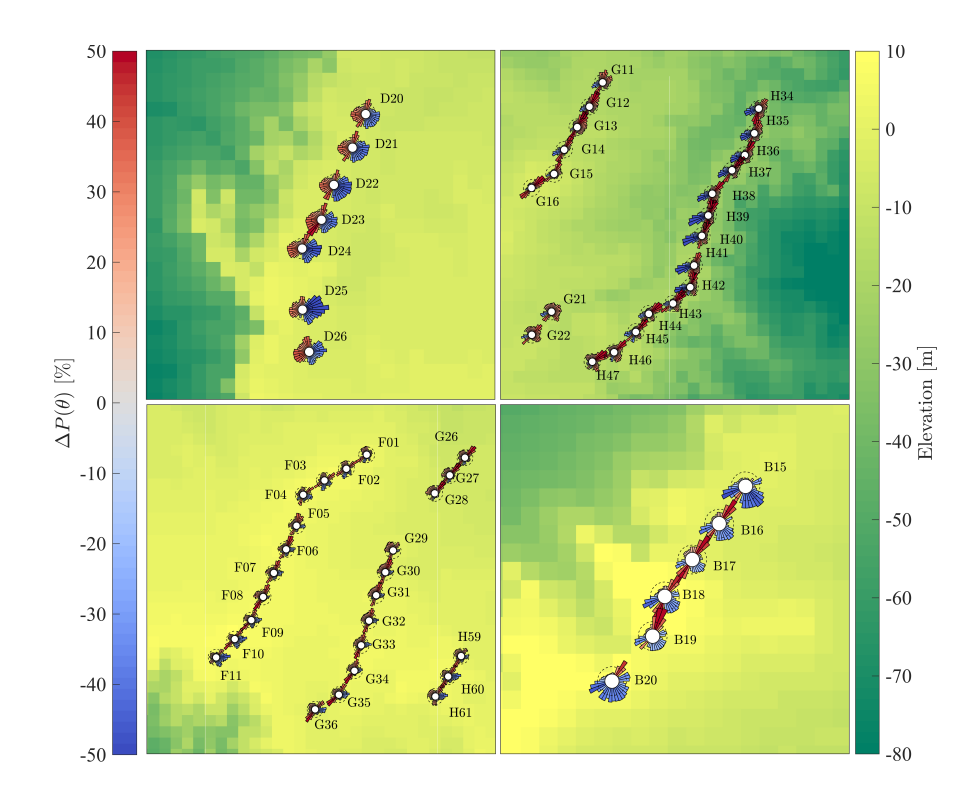


Figure 7. Average percentage power losses for  $U_{hub}^* \in (0.3, 1)$ : a) waked wind sectors; b) unwaked wind sector.

**1452** (2020) 012077

doi:10.1088/1742-6596/1452/1/012077



**Figure 8.** Directional power losses in specific areas of the wind farm. a) area I; b) area II; c) area III, d) area IV. The dashed circles indicate 20% loss (or gain).

that reduce the power available at the rotor for westerly wind directions. On the other side, the power gains occurring for the opposite wind sector suggest the presence of a speed-up that builds up on the plateau far from the escarpment. We are currently verifying such hypothesis through our LiDAR data and the preliminary results are encouraging.

Selection of Fig. 8 b includes Mitsubishi turbines installed close to the sharpest portion of the eastern escarpment and exhibits analogous features. Fig. 8 c highlights how in the center of the plateau the losses are dominated by turbine-to-turbine wake interactions, although these turbines share with the D row the power gain for easterly wind directions. Finally, the selected area in Fig. 8 d, corresponding to General Electric turbines facing west, sheds more light on the effect of topography on the flow within this wind farm. Here, in fact, turbine-to-turbine wake interaction is the only source of power loss, while a significant speed-up seems to occur for south-easterly wind. This confirms the possible acceleration that the plateau imparts to the flow in that wind sector. Surprisingly, the losses created by the escarpment and clearly observed in panel Fig. 8 b for a similar orientation are not present. The only difference between these two arrays is represented by the turbine model and hub height (GE turbines are 11 m taller than Mitsubishi). This is consistent with the formation of low momentum pockets generated by the escarpment that are confined at lower heights, thus affecting only the shortest turbines of row D.

A relevant quantity in the context of wind farm efficiency is the yearly energy loss. It is defined based on the dimensional power losses as:

$$\Delta E_i = \sum_j \Delta P_{dim,i}(\theta_j) \cdot p(\theta_i) \cdot 8760 \quad [\text{MWh/y}]$$
(9)

**1452** (2020) 012077

doi:10.1088/1742-6596/1452/1/012077

	GE	MHI	Escarpment
Waked	-18796 (-6.4%)	37952 (+4.72%)	
Unwaked	-6775 (-2.3 %)	7486 (+0.9%)	3032 (+4.2%)

**Table 3.** Yearly energy losses in MWH/y for different turbine models and for the turbines affected by the escarpment (D20-26 and H34-47). The value in brackets is the relative energy losses with respect to the total annual energy production of the specific cluster of turbines.

where  $p(\theta_i)$  is the probability of occurrence of the wind direction in the sector  $\theta_j \pm \Delta \theta/2$ , whereas the dimensional power losses  $\Delta P_{dim,i}$  are simply defined as the numerator of Eq. 7. The yearly energy losses (or gain) are reported in Table 3 for three clusters of turbines: General Electric, Mitsubishi and "Escarpment turbines". It is noteworthy how the speed-up detected for westerly winds significantly enhances the power capture of the GE turbines. The beneficial effect of topography overcomes the unavoidable turbine-to-turbine losses, as already observed in Fig. 8 d. On the other hand, the Mitsubishi turbines experience significant energy losses due to wake interaction as high as the 4% of their total energy yield, a value that is in agreement with previous studies [2, 5]. Still, losses from ideally unwaked wind sector represent 1% of the total energy production. Finally, we focused our attention to the turbines that appear to be more affected by the presence of the escarpment, specifically D20 to D26 and D34 to D47. In order to single out the detrimental effect of the escarpment, the losses reported in the third column of Table 3 consider only the western wind sector for D row and the eastern for H row. Based on the present model, the proximity to the escarpment is associated with an energy loss of more than 4% of the total production on an annual basis.

#### 5. Conclusion

LiDAR campaigns were carried out at two wind farms over flat and complex terrain. The first campaign encompasses more than 9,000 LiDAR PPI scans and simultaneous freestream measurements from met-tower and SCADA including hub height velocity and shear exponent. Upon non-dimensionalization and realignment of the PPI data, and via categorization of freestream parameters, we are able to generate clustered wake profiles through Barnes' scheme.

Reduction in near-wake velocity deficit due to the turbine setting is singled out, together with a faster wake recovery in convective/low shear exponent wind conditions. As a secondary trend, high thrust coefficient in region two of the power curve contributes to an enhanced wake recovery due to the wake-generated turbulence.

In the complex terrain, ensemble-averaged PPI scans show evidences of the speed up from topography and distortion on the velocity field, which is corroborated through a linear regression analysis against SCADA data. Freestream velocity and turbine power losses are estimated by coupling LiDAR and SCADA data. The power losses of the turbines in proximity of the escarpment reveal unexpected trend in power production due to the speed-up effect and disturbances from topography, while power losses of central arrays are related to wake interactions. The conditional sampling analysis of prevailing wind directions has further addressed such feature for downstream speed-up and upstream disturbances, where the latter is responsible for about 4% energy losses for the Mitsubishi turbines in proximity of the escarpment.

#### Acknowledgments

This research has been funded by a grant from the National Science Foundation CBET Fluid Dynamics, award number 1705837. This material is based upon work supported by the National Science Foundation under Grant Number IIP-1362022 (Collaborative Research: I/UCRC for Wind Energy, Science, Technology, and Research) and from the WindSTAR I/UCRC Members:

**1452** (2020) 012077 doi:10.1088/1742-6596/1452/1/012077

Aquanis, Inc., EDP Renewables, Bachmann Electronic Corp., GE Energy, Huntsman, Hexion, Leeward Asset Management, LLC, Pattern Energy, and TPI Composites. Any opinions, findings, and conclusions or recommendations expressed in this material are those of the authors and do not necessarily reflect the views of the sponsors.

#### 6. References

- [1] Barthelmie RJ, Hansen KS, Frandsen ST, Rathmann O, Schepers JG, Schlez W, Philips J, Rados K, Zervos A, Politis ES, et al.. Modelling and measuring flow and wind turbine wakes in large wind farms offshore, Wind Energy 2009; 12 (5), 431-444.
- [2] El-Asha S, Zhan L, Iungo GV. Quantification of power losses due to wind turbine wake interactions through SCADA, meteorological and wind LiDAR data. Wind Energy 2017; 1823-1839.
- [3] Santhanagopalan V, Rotea MA, Iungo GV. Performance optimization of a wind turbine column for different incoming wind turbulence. *Renewable Energy*. 2018; 116: 232-243.
- [4] Iungo GV, Santhanagopalan V, Ciri U, Viola F, Zhan L, Rotea MA, Leonardi S. Parabolic RANS solver for low-computational-cost simulations of wind turbine wakes. Wind Energy. 2018; 21(3): 184-197.
- [5] Santhanagopalan V, Letizia S, Zhan L, Al-Hamidi LY, Iungo GV. Profitability optimization of a wind power plant performed through different optimization algorithms and a data-driven RANS solver. 2018 Wind Energ. Symp., AIAA SciTECH. 2018: 2018-2018.
- [6] Hansen KS, Barthelmie RJ, Jensen LE, Sommer A. The impact of turbulence intensity and atmospheric stability on power deficits due to wind turbine wakes at Horns Rev wind farm. Wind Energy 2012; 15, 183-196.
- [7] Iungo GV, Porte-Agel F. Volumetric lidar scanning of wind turbine wakes under convective and neutral atmospheric stability regimes. J. Ocean. Atmos. Technol. 2014; 31 (10), 2035-2048.
- [8] Barthelmie RJ, Rathmann O, Frandsen ST, Hansen K, Politis E, Prospathopoulos J, Rados K, Cabézon D, Schlez W, Phillips J, Neubert A, Schepers JG, van der Pijl SP. Modelling and measuring of wakes in large wind farms. J. Phys.: Conf. Ser. 2007; 75, 012049.
- [9] Fernando HJS, Mann J, Palma JMLM, Lundquist JK, Barthelmie RJ, Belo-Pereira M, Brown WOJ, Chow FK, Gerz T, Hocut CM et al. The Perdigão: Peering into Microscale Details of Mountain Winds, Bulletin of American Meteorological Society (2019), early release
- [10] IEC 61400-12-1 Ed 2.0: Wind turbines Part 12-1: power performance measurements of electricity producing wind turbines, IEC, Geneva, Switzerland, 2015.
- [11] U.S. Geological Survey Website, last access on October 31, 2017, https://www.usgs.gov/.
- [12] Jensen NO. A note on wind generator interaction, Risø-M 1983; No. 2411.
- [13] Barnes SL. A technique for maximizing details in numerical weather map analysis. J. Appl. Meteorol. 1964; 3 (4): 396-409.
- [14] Newsom RK, Brewer WA, Wilczak JM, Wolfe DE, Oncley SP, Lundquist JK. Validating precision estimates in horizontal wind measurements from a Doppler lidar. *Atmos. Meas. Tech.* 2017; 10 (3): 1229-1240.
- [15] Bastankhah M, Porté-Agel F. A new analytical model for wind-turbine wakes. Renewable Energy. 2014;70: 116-23.
- [16] Iungo GV, Viola F, Camarri S, Porté-Agel F, Gallaire F. Linear stability analysis of wind turbine wakes performed on wind tunnel measurements. J. Fluid Mech. 737(2013):499-526.
- [17] Viola F, Iungo GV, Camarri S, Porté-Agel F, Gallaire F. Prediction of the hub vortex instability in a wind turbine wake: stability analysis with eddy-viscosity models calibrated on wind tunnel data. J. Fluid Mech. 2014 Jul;750.
- [18] Ashton R, Viola F, Camarri S, Gallaire F, Iungo GV. Hub vortex instability within wind turbine wakes: Effects of wind turbulence, loading conditions, and blade aerodynamics. *Phys. Rev. Fluids.* 2016; 1(7): 073603.
- [19] Astolfi D, Castellani F. and Terzi L. Definition and Interpretation of Wind Farm Efficiency in Complex Terrain: A Discussion. *J. Energ. Resour.* 2019; 141(5): 055501.
- [20] Castellani F, Astolfi D, Terzi L, Hansen KS, Rodrigo JS. Analysing wind farm efficiency on complex terrains. J. Phys.: Conf. Ser.. 2014; 524(1): 012142.
- [21] Katic I, Højstrup J and Jensen NO. A simple model for cluster efficiency. European Wind Energy Association Conference and Exhibition Rome. 1986; 1:407-410.
- [22] Peña A, Réthoré PE, van der Laan MP. On the application of the Jensen wake model using a turbulence-dependent wake decay coefficient: the Sexbierum case. Wind Energy. 2016; 19(4): 763-776.